Research Article | Vol. 25, No. 25 | 11 Dec 2017 | OPTICS EXPRESS 31651
Optics EXPRESS

Experimental study of the sensitivity of a porous silicon ring resonator sensor using continuous in-flow measurements

RAFFAELE CAROSELLI,[1] SALVADOR PONCE-ALCÁNTARA,[1] FRANCISCO PRATS QUILEZ,[1] DAVID MARTÍN SÁNCHEZ,[1] LUIS TORRIJOS MORÁN,[1] AMADEU GRIOL BARRES,[1] LAURENT BELLIERES,[1] HANNA BANDARENKA,[2] KSENIYA GIREL,[2] VITALY BONDARENKO,[2] AND JAIME GARCÍA-RUPÉREZ[1,*]

[1]*Nanophotonics Technology Center, Universitat Politècnica de València, Camino de Vera s/n, 46022 Valencia, Spain*
[2]*Micro- and Nanoelectronics Department, Belarusian State University of Informatics and Radioelectronics, P. Brovka str. 6, 220013 Minsk, Belarus*
[*]*jaigarru@ntc.upv.es*

Abstract: A highly sensitive photonic sensor based on a porous silicon ring resonator was developed and experimentally characterized. The photonic sensing structure was fabricated by exploiting a porous silicon double layer, where the top layer of a low porosity was used to form photonic elements by e-beam lithography and the bottom layer of a high porosity was used to confine light in the vertical direction. The sensing performance of the ring resonator sensor based on porous silicon was compared for the different resonances within the analyzed wavelength range both for transverse-electric and transverse-magnetic polarizations. We determined that a sensitivity up to 439 nm/RIU for low refractive index changes can be achieved depending on the optical field distribution given by each resonance/polarization.

OCIS codes: (130.3120) Integrated optics devices; (130.6010) Sensors; (230.5750) Resonators.

References and links

1. M. C. Estevez, M. Alvarez, and L. M. Lechuga, "Integrated optical devices for lab-on-a-chip biosensing applications," Laser Photonics Rev. **6**(4), 463–487 (2012).
2. D.-X. Xu, A. Densmore, A. Delâge, P. Waldron, R. McKinnon, S. Janz, J. Lapointe, G. Lopinski, T. Mischki, E. Post, P. Cheben, and J. H. Schmid, "Folded cavity SOI microring sensors for high sensitivity and real time measurement of biomolecular binding," Opt. Express **16**(19), 15137–15148 (2008).
3. M. S. Luchansky and R. C. Bailey, "High-Q optical sensors for chemical and biological analysis," Anal. Chem. **84**(2), 793–821 (2012).
4. K. De Vos, I. Bartolozzi, E. Schacht, P. Bienstman, and R. Baets, "Silicon-on-Insulator microring resonator for sensitive and label-free biosensing," Opt. Express **15**(12), 7610–7615 (2007).
5. A. L. Washburn, L. C. Gunn, and R. C. Bailey, "Label-free quantitation of a cancer biomarker in complex media using silicon photonic microring resonators," Anal. Chem. **81**(22), 9499–9506 (2009).
6. Genalyte, Inc., http://www.genalyte.com/
7. M. Iqbal, M. A. Gleeson, B. Spaugh, F. Tybor, W. G. Gunn, M. Hochberg, T. Baehr-Jones, R. C. Bailey, and L. C. Gunn, "Label-free biosensor arrays based on silicon ring resonators and high speed optical scanning instrumentation," IEEE J. Sel. Top. Quantum Electron. **16**(3), 654–661 (2010).
8. T. Claes, J. G. Molera, K. De Vos, E. Schachtb, R. Baets, and P. Bienstman, "Label-free biosensing with a slot waveguide-based ring resonator in silicon on insulator," IEEE Photonics J. **1**, 197–204 (2009).
9. S. T. Fard, V. Donzella, S. A. Schmidt, J. Flueckiger, S. M. Grist, P. Talebi Fard, Y. Wu, R. J. Bojko, E. Kwok, N. A. F. Jaeger, D. M. Ratner, and L. Chrostowski, "Performance of ultra-thin SOI-based resonators for sensing applications," Opt. Express **22**(12), 14166–14179 (2014).
10. J. Flueckiger, S. Schmidt, V. Donzella, A. Sherwali, D. M. Ratner, L. Chrostowski, and K. C. Cheung, "Sub-wavelength grating for enhanced ring resonator biosensor," Opt. Express **24**(14), 15672–15686 (2016).
11. V. Yakovtseva, V. Bondarenko, M. Balucani, N. Kazuchits, and A. Ferrari, "Integrated optical waveguides based on porous silicon: state-of-the-art and outlook for progress," Physics, Chemistry and Application of Nanostructures **99**, 375–377 (1999).
12. S. Dhanekar and S. Jain, "Porous silicon biosensor: Current status," Biosens. Bioelectron. **41**(1), 54–64 (2013).
13. P. A. Snow, E. K. Squire, P. S. J. Russell, and L. T. Canham, "Vapor sensing using the optical properties of porous silicon Bragg mirrors," J. Appl. Phys. **86**(4), 1781–1784 (1999).

#306445 https://doi.org/10.1364/OE.25.031651
Journal © 2017 Received 6 Sep 2017; revised 2 Nov 2017; accepted 4 Nov 2017; published 5 Dec 2017

Optics EXPRESS

14. C. Baratto, G. Faglia, E. Comini, G. Sberveglieri, A. Taroni, V. La Ferrara, L. Quercia, and G. Di Francia, "A novel porous silicon sensor for detection of sub-ppm NO_2 concentrations," Sens. Actuators B Chem. **77**(1–2), 62–66 (2001).
15. L. De Stefano, L. Rotiroti, I. Rea, L. Moretti, G. Di Francia, E. Massera, A. Lamberti, P. Arcari, C. Sanges, and I. Rendina, "Porous silicon-based optical biochips," J. Opt. A, Pure Appl. Opt. **8**(7), S540–S544 (2006).
16. H. Zhang, Z. Jia, X. Lv, J. Zhou, L. Chen, R. Liu, and J. Ma, "Porous silicon optical microcavity biosensor on silicon-on-insulator wafer for sensitive DNA detection," Biosens. Bioelectron. **44**, 89–94 (2013).
17. K. Kim and T. E. Murphy, "Porous silicon integrated Mach-Zehnder interferometer waveguide for biological and chemical sensing," Opt. Express **21**(17), 19488–19497 (2013).
18. G. A. Rodriguez, S. Hu, and S. M. Weiss, "Porous silicon ring resonator for compact, high sensitivity biosensing applications," Opt. Express **23**(6), 7111–7119 (2015).
19. F. A. Harraz, "Porous silicon chemical sensors and biosensors: A review," Sens. Actuators B Chem. **202**, 897–912 (2014).
20. O. Bisi, S. Ossicini, and L. Pavesi, "Porous silicon: A quantum sponge structure for silicon based optoelectronics," Surf. Sci. Rep. **38**(1), 1–126 (2000).
21. D. A. G. Bruggeman, "Dielectric constant and conductivity of mixtures of isotropic materials," Ann. Phys. **24**, 636–679 (1935).
22. R. B. Balili, "Transfer matrix method in nanophotonics," Int. J. Mod. Phys. Conf. Ser. **17**, 159–168 (2012).
23. L. Pavesi, "Porous silicon dielectric multilayers and microcavities," Riv. Nuovo Cim. **20**(10), 1–76 (1997).
24. W. S. Rasband, "ImageJ", https://imagej.nih.gov/ij/.

1. Introduction

Optical ring resonators (RRs) are probably the planar photonic structures mostly employed for the development of sensing devices due to their structural simplicity, compact size and high sensitivity. Many research groups and commercial companies have demonstrated strong activity in the development of RR arrays for the highly sensitive and multiplexed detection of analytes for different applications [1–6]. Nowadays, a traditional Silicon-on-Insulator (SOI) RRs can provide sensitivities up to around 160 nm/RIU (Refractive Index Units) [7]. However, the performance of traditional planar photonic sensing structures based on a configuration with a high refractive index (RI) contrast is limited by the fact that only the evanescent field propagating outside of the photonic structure is used for sensing purposes, while the majority of the optical field distribution associated with the guided mode propagates within the structure itself. Novel RR configurations have been proposed to overcome this limitation, as those based on slot waveguides [8], on ultra-thin SOI substrates [9] or on sub-wavelength waveguides [10]. Another option to increase the sensitivity, which is considered in this work, is the use of porous silicon (PS) for the development of the sensing structures. The high potential of porous silicon for sensing purposes, what has been demonstrated in several works [11–18], comes from the possibility of infiltrating the target analytes directly into the pores in order to obtain a significantly improved sensitivity [19]. Additionally, PS is characterized by a very high surface-to-volume ratio [20], what allows immobilizing a significantly larger amount of bioreceptors over the inner walls of the pores for the better detection of biorecognition events. Moreover, PS can be formed simply, quickly and inexpensively since it is the result of the electrochemical etching of a silicon substrate.

In this work, we study the sensing performance of a porous silicon ring resonator (PSRR) sensor for transverse-electric (TE) and transverse-magnetic (TM) polarizations. In case of each polarization, we measured the sensitivity for every resonance within the analyzed wavelength range, which is determined by the optical field distribution of the PSRR resonant mode and its interaction with the medium filling the pores. Experimental results obtained by flowing several ethanol-water dilutions over the porous structure provided a sensitivity up to 439 nm/RIU for the low ethanol concentrations when working with TE-polarized light.

2. Fabrication of the PSRR

First, we selected the RI profile of the double-layered PS to be used, aiming at having a strong light confinement in the top layer, where the photonic sensing structures will be patterned. To reach this goal, the RI contrast between the top and bottom layers of PS needs to be as high as possible when water is infiltrated into the pores. However, there is a

Optics EXPRESS

limitation in the maximum reduction of the RI of the bottom layer since it implies increasing the porosity of this PS layer, what compromises the stability of the photonic structure. Taking these considerations into account, we selected porosities of the top and bottom PS layers of 35% and 65%, respectively. By using the Bruggeman equation [21], we determined the RI of the PS layers for these porosities, being $n_{top\text{-}water} = 2.67$ and $n_{lc\text{-}water} = 1.95$ when considering water-filled pores, and $n_{top\text{-}air} = 2.56$ and $n_{lc\text{-}air} = 1.7$ when considering air-filled pores.

The designed double-layered PS was fabricated by an electrochemical etching of a single-side polished boron doped (resistivity of 0.01 – 0.02 Ω·cm) <100> Si wafer, in a solution of 48% hydrofluoric acid and 99% ethanol mixed in a 1:2 volume ration. Just before the etching process, the silicon wafer was cleaned from possible organic residues using a piranha solution (volume ration H_2SO_4:H_2O_2 = 3:1) and then immersed into aqueous solution of HF (5%) to remove SiO_2 from the surface. After each cleaning step, the wafer was rinsed in deionized water (DIW). The top layer with high RI was formed by applying a current density of 5 mA/cm^2 for 100 seconds and the bottom layer of 45 mA/cm^2 for 110 seconds. The cleaning procedures and the electrochemical etching were performed at room temperature. The fabricated PS sample was washed with acetone, isopropyl alcohol and DIW to remove residual surface impurities. Finally, an O_2 plasma was applied for 6 minutes, in order to improve the hydrophilicity of the PS surface.

The fabricated PS sample was cleaved into two parts: one for the physical characterization of the PS layers and the other one for the fabrication of the photonic structures. Field emission scanning electron microscope (FE-SEM) was used to study the thickness and the uniformity of both PS layers as well as the average pore diameter of the top PS layer. Figure 1(a) shows a FE-SEM image of the cross section of the double-layered PS, where the different porosities of both layers are clearly distinguished. The measured thicknesses for the top and bottom PS layers were around 800 nm and 4350 nm, respectively. Refractive indices of the double-layer were calculated from Fresnel coefficients under the Transfer Matrix Method approach using reflection measurements of the porous structure [22, 23]. In this respect, the refractive indices obtained were $n_{top\text{-}air} = 2.48$ and $n_{lc\text{-}air} = 1.75$ for the air-filled pores, what corresponds to porosities of 38% and 63%, respectively. These porosities are practically identical to those previously selected in the design phase, thus indicating a good control of the PS fabrication procedure. Additionally, the ImageJ software [24] was used to analyse a top-view FE-SEM image, shown in Fig. 1(b), in order to obtain the average pore diameter of the sensing structure, which was determined to be around 12 nm.

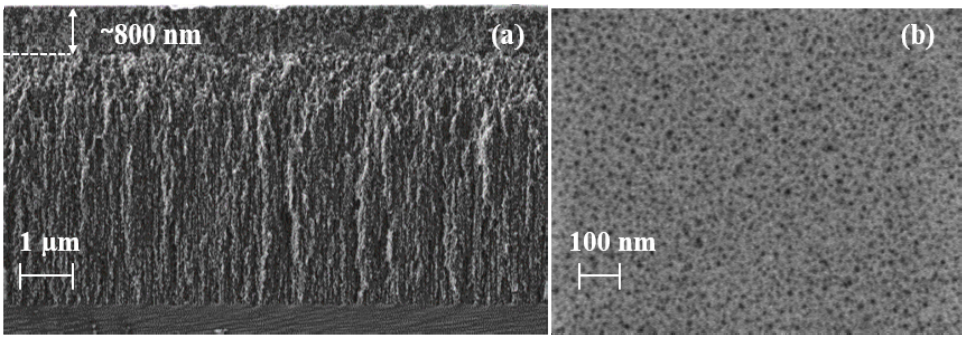

Fig. 1. FE-SEM images of (a) cross section and (b) top-view of the PS structure.

Finally, a lithographic process was used to create the planar photonic structures in the top PS layer. Designs were patterned into a PMMA positive resist layer using e-beam lithography with an acceleration voltage of 10 keV and a dose of ~87 µC/cm^2. Then, after developing the resist, the pattern was transferred to the top PS layer by inductively coupled plasma (ICP) etching. The fabricated design consisted of a 20µm-radius RR coupled to a coupling waveguide. Several sets of this structure were fabricated using different widths of the

Optics EXPRESS

coupling and the RR waveguides (800, 1000 and 1200 nm) and different coupling gaps between the coupling waveguide and the RR (150, 200, 250, 300 and 350 nm). In order to ease the butt-coupling characterization of the photonic structures, the coupling waveguide was tapered to a width of 10 µm at the edges of the chip. Figure 2 shows several FE-SEM images of the fabricated structures.

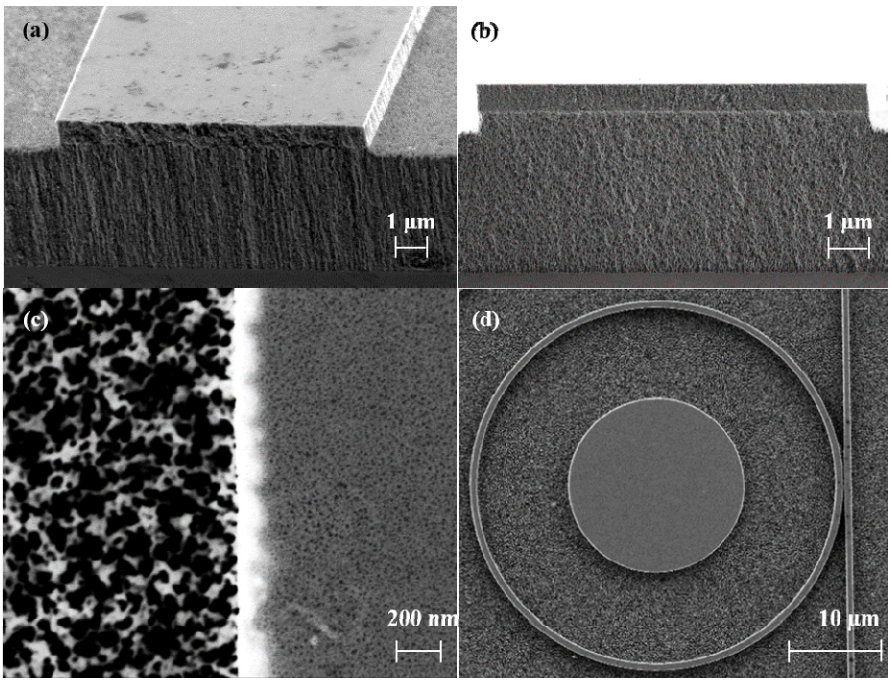

Fig. 2. FE-SEM images of the fabricated PSRR chip. (a) 60°-sectional image of the 10µm-wide access waveguide. Thanks to the vertical cut of this sample edge, the vertical orientation of the pores can be observed. (b) Cross-sectional image of the 10µm-wide access waveguide. Thanks to the non-vertical cut of this sample edge, the sponge-like morphology of the PS and the boundary between the two PS layers can be clearly observed. (c) Top-view image of the top and bottom PS layers in the access waveguide region, where the porosity difference between them can be clearly observed. (d) Top-view image of the RR and the coupling waveguide.

3. Experimental setup and static characterization of the PSRR

An opto-fluidic setup, which is shown in Fig. 3, was developed to carry out the optical characterization of the PSRR and the RI detection experiments. The optical part of the setup consisted in a horizontal coupling interrogation platform where the light from a continuous sweep tunable laser (Keysight 81980A) was coupled to the access waveguides in the PSRR chip using a lensed fiber. The polarization of the input light was adjusted using a polarization controller (Thorlabs FPC562) before injecting it into the chip. The light coming out from the PSRR chip was collected with an objective (20X Olympus Plan Achromat, 0.4 NA) and passed through a polarizer (Newport RM25A) in order to measure the signal level for the selected polarization using an infrared (IR) camera (Xenics Xeva-1.7-320). The interrogation platform was controlled using a software programmed in LabVIEW able to synchronize the continuous sweep of the laser with the image acquisition of the IR camera via a trigger signal in order to obtain the spectrum of the photonic structure with the desired spectral resolution.

Regarding the fluidic part of the setup, a microfluidic delivery system made in polydimethylsiloxane (PDMS) was placed on top of the chip in order to flow all the solutions over the sensing structure. A Finetech flip-chip tool was used to properly align the fluidic microchannel with the PSRR structures. When the experiments were carried out, the target

Optics EXPRESS

solutions were flowed using a syringe pump working in withdraw mode and set to a constant flow rate of 20 µl/min. By working in withdraw mode, the liquid flowed through the PDMS channel can be easily changed by simply changing the vial at the end of the tubing.

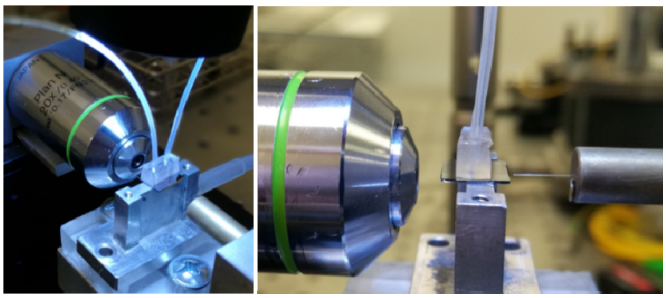

Fig. 3. Pictures of the fiber-to-camera horizontal interrogation setup. The PDMS microfluidic flow cell on top of the photonic chip can be also observed.

After characterizing in water environment the TE and TM spectra for all the configurations included in the photonic chip (i.e., different waveguide widths and coupling gaps), we determined that the best spectral responses in terms of resonances quality and optical losses were obtained for the configuration having a coupling waveguide width of 1000 nm and a coupling gap of 200 nm. Figure 4 shows the measured TE and TM spectra, in water environment, for that PSRR configuration. The average quality factor of the measured resonances is quite reduced (453 and 512 for TE and TM polarizations, respectively) due to the higher losses that are produced in the PS-based waveguides compared to typical solid core ones. The inset images in Fig. 4 represent the light spots acquired with the IR camera at the 10µm-wide output waveguide for each polarization. It is possible to appreciate that a better confined mode is obtained for TE polarization, while a higher amount of light is going into the lower cladding for TM polarization.

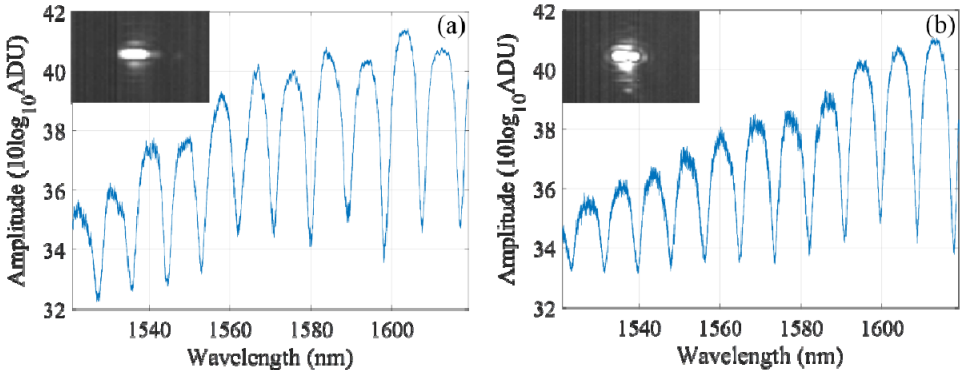

Fig. 4. Spectra of the PSRR for (a) TE and (b) TM polarization. The amplitude is represented in terms of the analog-to-digital units (ADU) measured by the camera (in logarithmic scale). The inset in each graph shows the measured optical profile at the output waveguide for each polarization.

The selected waveguide configuration was simulated using the software FemSIM in order to determine the modes existing on it for a water environment. Two fully propagating modes were obtained for that waveguide configuration for each polarization, while a third mode also begins to propagate for both polarizations. The field profiles of those modes are shown in Fig. 5. From the optical profiles measured in the experiments, which were depicted in Fig. 4 we can see that only the fundamental mode is properly excited and propagated for TE polarization, while higher order modes are excited and propagated for TM polarization, leading to a higher delocalization of the optical field.

Optics EXPRESS

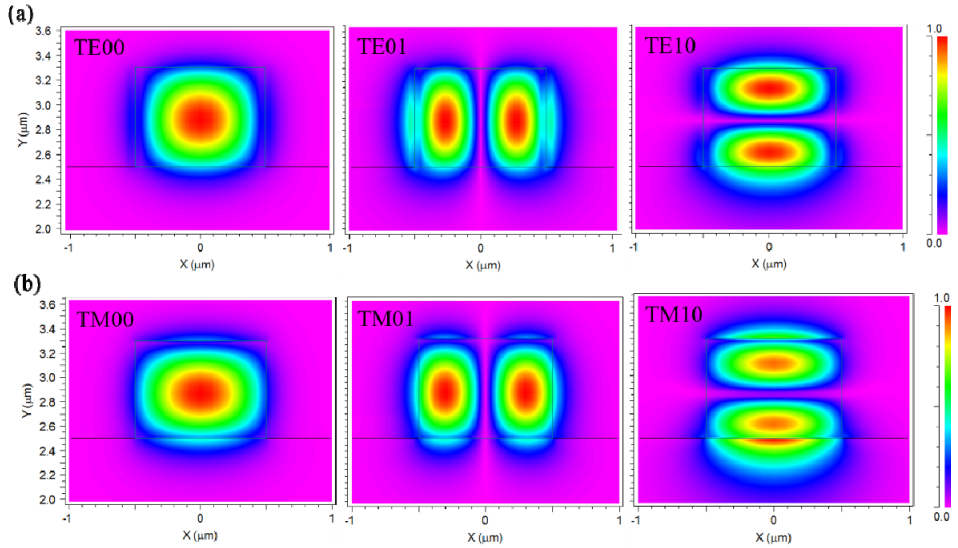

Fig. 5. Simulations of the optical modes propagating in the selected PS waveguide configuration (height = 800 nm and width = 1000 nm) for (a) TE and (b) TM polarization. The modes are ordered from left to right.

4. PSRR sensitivity characterization

Several RI sensing experiments were performed to determine the sensitivity of the photonic structure. To this aim, different ethanol-water dilutions were flowed over the sensor while the transmission spectrum was continuously acquired in order to determine the shift of the PSRR resonances. The ethanol (EtOH) concentrations in DIW used in the experiments were 10%, 5% and 1%, which correspond to RI changes of $6.6 \cdot 10^{-3}$, $3.3 \cdot 10^{-3}$ and $6.6 \cdot 10^{-4}$ RIU respect DIW, respectively. For the spectra acquisition, the tunable laser was swept from 1520 to 1620 nm with a sweeping speed of 10 nm/s (the total time for each sweep is 10 seconds) and the synchronization with the IR camera provided a spectral resolution of 20 pm. A Lorentzian fitting of each resonance was then performed in Matlab to determine its position with a higher accuracy. All the experiments were carried out for TE and TM polarizations.

Figures 6(a) and 6(b) show the time evolution for the most and least sensitive PSRR resonances within the sweeping range for TE and TM polarizations, respectively. As it can be observed in these figures, the resonances presented a similar behavior for both polarizations and only a slightly higher sensitivity is obtained for TE polarization resonances. This is related to the fact that the sensing occurs mainly inside the guiding structures, where the field distribution is similar in both cases. However, since a better light confinement is obtained for TE polarization, as it was shown in the spot images presented in Fig. 4, a higher sensitivity is provided by this polarization. This is the opposite to what typically happens for evanescent wave sensors, where TM modes are generally more sensitive because of the presence of a higher amount of evanescent field over the top surface of the structure. The average sensitivity of the PSRR sensor (i.e., for all the resonances within the measured range) is around 350 nm/RIU for TE and 320 nm/RIU for TM when considering the whole range of refractive index variations that has been measured. The maximum sensitivity value, around 380 nm/RIU, was provided by the resonance located at ~1607.5 nm for TE polarization, whose quality factor is 513. Such values are more than twice higher than the sensitivity achieved for a traditional SOI RR. The noise level measured for all the resonances is below 1 pm, reaching values even in the range of 0.1 pm for some resonances as it is depicted in the inset of Fig. 6(a). Finally, note that the time required by the resonances to reach the plateau

Optics EXPRESS

for each flowed substance (around 1 minute) is determined by the diffusion that is produced in the input tubing at the interface between the liquids.

Figure 7 represents the spectral shift measured for each resonance for both polarizations, where an oscillatory-like behavior can be observed as we move towards higher order resonances. This sensitivity variation indicates that a different interaction between the resonance optical modes and the target substance is taking place, which might be determined by the local variations of the pores properties and distribution of the fabricated PS layer where the RR is created. Besides that oscillatory-like behavior, the average shift also increases as a function of the wavelength, due to the larger evanescent field of the modes as wavelength is increased.

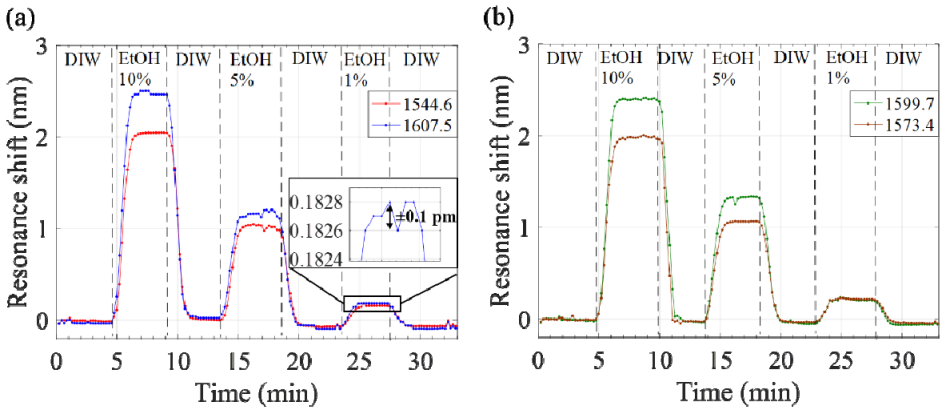

Fig. 6. Time evolution of the resonance shift for (a) TE polarization and (b) TM polarization when flowing three cycles of EtOH in DIW with concentrations 10%, 5% and 1% (meaning RI changes of $6.6\cdot10^{-3}$, $3.3\cdot10^{-3}$ and $6.6\cdot10^{-4}$ RIU respect DIW, respectively) with cycles of DIW flow between them. The different colors indicate the different resonances within the measured wavelength range being tracked.

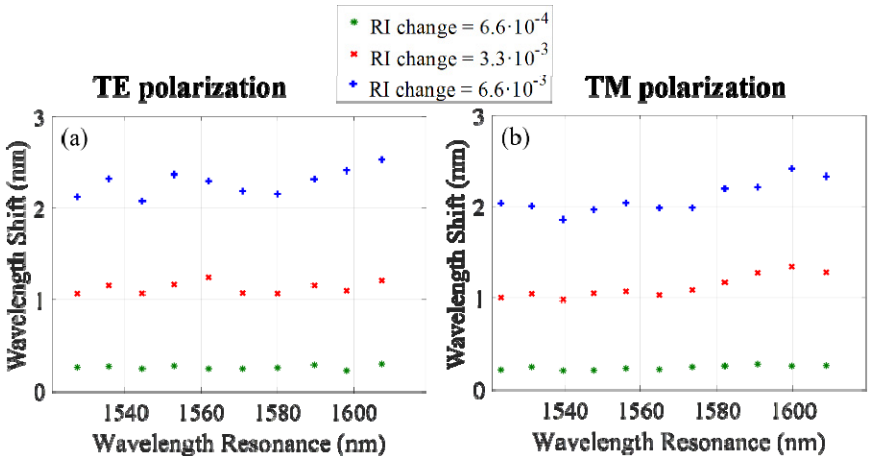

Fig. 7. Wavelength shift of each resonance for each RI variation for (a) TE and (b) TM polarizations.

In Fig. 8, the sensitivity curves of each resonance for TE and TM polarizations are shown. As it can be observed, the sensitivity behavior of the PSRR sensing structure was not totally linear. In fact, the sensor exhibited a higher sensitivity for lower RI variations, specifically, for RI variation of $6.6\cdot10^{-4}$ RIU corresponding to the EtOH 1% concentration. This is related with the non-linear variation of the RI of the top porous layer that is produced when changing

Optics EXPRESS

the RI of the solution infiltrated into the pores, as it is shown in Fig. 9. We can see that a higher variation of the effective refractive index of the top layer is obtained for the EtOH 1% concentration than for the EtOH 5% and 10% concentrations. For this reason, the PS structure showed a higher sensitivity for such EtOH concentration. Thanks to such behavior, the highest sensitivity value provided by the PSRR sensor was 439 nm/RIU for the TE resonance located at ~1607.5 nm when considering a RI variation of $6.6 \cdot 10^{-4}$ RIU.

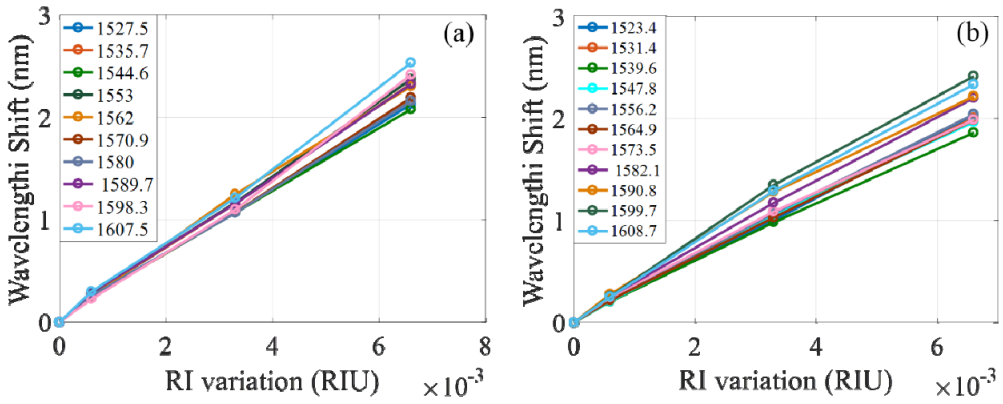

Fig. 8. Sensitivity curve of each resonance for (a) TE and (b) TM polarizations.

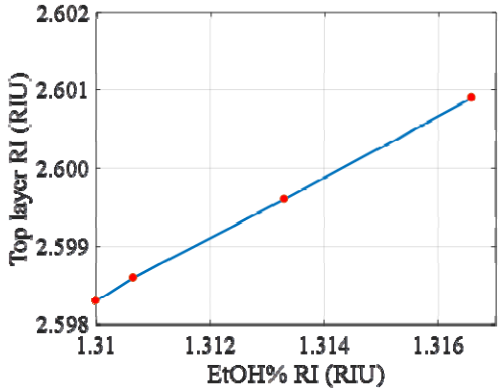

Fig. 9. Top PS layer RI variation as a function of the EtOH solution RI.

5. Conclusions

A highly sensitive PSRR was developed thanks to the formation of a PS double layer with a high RI contrast and its sensing performance was characterized both for TE and TM polarizations. The characterization was performed by monitoring in continuum the evolution of the sensing structure spectrum. The experimental results indicate that the sensitivity of the PSRR was slightly better for the TE polarization than for the TM polarization. This is because the sensing occurs in the core of the structure, where the TE polarization plays a major influence due to the better confinement of the light in the photonic structure. Working with such polarization, a sensitivity of 439 nm/RIU was achieved for the detection of low RI variations. The higher light-matter interaction that is produced due to the fact that the sensing occurs directly inside the structure, together with the possibility of immobilizing the bioreceptors on the inner surface of the pores, make PS a suitable platform for the development of new biosensing devices exhibiting a high sensitivity. Finally, note that the combination of PS substrates with some of the configurations that have been proposed to increase the sensitivity of photonic structures as slot or sub-wavelength waveguides might provide even higher sensitivities.

Optics EXPRESS

Funding

European Commission through the project H2020-644242 SAPHELY; Spanish government through the projects TEC2013-49987-EXP BIOGATE and TEC2015-63838-C3-1-R-OPTONANOSENS; Generalitat Valenciana through the Doctoral Scholarship GRISOLIAP/2014/109.